Geochemistry, Geophysics, Geosystems®

AGU ADVANCING EARTH AND SPACE SCIENCE

RESEARCH ARTICLE
10.1029/2023GC010879

# Metal Preservation and Mobilization in Sediments at the TAG Hydrothermal Field, Mid-Atlantic Ridge

**Adeline Marie Dutrieux[1], Anna Lichtschlag[2], Fernando J. A. S. Barriga[3], Sofia Martins[3], Jelena Milinovic[3,4], and Bramley J. Murton[2]**

[1]School of Ocean and Earth Science, University of Southampton, Southampton, UK, [2]National Oceanography Centre, Southampton, UK, [3]Departamento de Geologia, Faculdade de Ciências, Instituto Dom Luíz, Universidade de Lisboa, Lisboa, Portugal, [4]Department of Chemistry and Biochemistry, Faculty of Sciences, CIQ-UP, Institute of Molecular Sciences (IMS), University of Porto, Porto, Portugal

**Key Points:**

- TAG hydrothermal field sediments have high metal contents that vary distinctly between different seafloor depositional environments
- Lowest metal contents are found in sediments on top and highest in those at the base of extinct hydrothermal mounds
- Deposition, remobilization, and preservation of metals in hydrothermal sediments lead to distinctively different sediment characteristics

**Supporting Information:**

Supporting Information may be found in the online version of this article.

**Correspondence to:**

A. Lichtschlag,
Anna.Lichtschlag@noc.ac.uk

**Citation:**

Dutrieux, A. M., Lichtschlag, A., Barriga, F. J. A. S., Martins, S., Milinovic, J., & Murton, B. J. (2023). Metal preservation and mobilization in sediments at the TAG hydrothermal field, Mid-Atlantic Ridge. *Geochemistry, Geophysics, Geosystems*, *24*, e2023GC010879. https://doi.org/10.1029/2023GC010879

Received 30 JAN 2023
Accepted 20 APR 2023

**Author Contributions:**

**Conceptualization:** Adeline Marie Dutrieux, Anna Lichtschlag, Fernando J. A. S. Barriga, Jelena Milinovic, Bramley J. Murton
**Data curation:** Adeline Marie Dutrieux
**Formal analysis:** Adeline Marie Dutrieux, Sofia Martins, Jelena Milinovic
**Funding acquisition:** Fernando J. A. S. Barriga, Bramley J. Murton
**Investigation:** Adeline Marie Dutrieux, Sofia Martins



**Abstract** At the Trans-Atlantic Geotraverse hydrothermal field, metalliferous sediments cover extinct hydrothermal mounds and the surrounding seafloor. Here, we report the morphological, mineralogical and geochemical processes that deposit these sediments, remobilize their metals, and affect their preservation. We found that the initial sediment metal tenor is controlled by physical transport of hydrothermal material from its source, followed by diagenetic redistribution and potentially diffuse fluid flow after high-temperature hydrothermal activity has ceased. We distinguished three different environments: (a) proximal metalliferous sediments on top of extinct mounds are mainly derived from oxidative weathering of primary sulfide structures and are predominantly composed of Fe oxyhydroxides with low contents of Cu, Co, and Zn; metal enrichments in specific layers are likely related to upward flow of low-temperature hydrothermal fluids; (b) medial distant metalliferous sediments found at the base of the mounds, deposited by mass transport, contain cm-thick layers of unsorted sulfide sands with high base metal contents (e.g., up to 28% Cu); these buried sulfides continue to undergo dissolution, resulting in metal release into porewaters; (c) distal metalliferous sediments, found in depositional basins a few hundreds of meters from the extinct mounds, include fining-upwards sequences of thin sulfide sand layers with Fe oxyhydroxides and were deposited by recurrent turbiditic flows. Dissolved metals (e.g., $Cu^{2+}$ and $Mn^{2+}$) diffuse upwards under reducing conditions and precipitate within the sediment. Hence, when using hydrothermal sediments to construct reliable geochronological records of hydrothermal activity, distance from source, local seafloor morphology, mass-transport and depositional, and diagenetic modification should all be considered.

**Plain Language Summary** The seafloor massive sulfide mounds at the TAG hydrothermal field (Mid-Atlantic Ridge) are surrounded by metalliferous sediments. These sediments can be used to understand the history of the hydrothermal activity; however, the evolution of these sediments can be complex. The aim of this study is to understand the processes that lead to the accumulation and alteration of these sediments. For this, we identified the mineralogical, geochemical and physical processes that affect the sediments. Our results show that sediments found on mound tops are mainly composed of iron and manganese oxides and hydroxides, and are low in other metal contents compared to other environments. Medial distant sediments at the base of the mounds have thick beds of sulfide-rich sediments that contain the highest concentrations of metals and are currently undergoing dissolution. In depositional channels, several hundreds of meters distal from the mounds, metalliferous sediment have accumulated in several meters thick layers that contain high concentrations of dissolved metals. This study reveals that the metal content of hydrothermal sediments is strongly controlled by their physicochemical environment and processes after deposition, and we suggest these processes should be considered when using metalliferous sediments as records of the evolution and activity of hydrothermal systems.

## 1. Introduction

Hydrothermal sediments are characterized by high concentrations of metals, mainly Fe and Mn, but also Cu, Zn, and Au, originating from hydrothermal sources (Gurvich, 2006; Shearme et al., 1983). In the ocean, these metal-rich sediments form in the vicinity of seafloor hydrothermal systems, for example, in back-arc basins and at mid-oceanic ridges (Gurvich, 2006; Hannington et al., 2011). A number of different hydrothermal processes are known to generate these metalliferous sediments, including the settling of primary hydrothermal plume particles,

**Methodology:** Adeline Marie Dutrieux, Sofia Martins
**Resources:** Anna Lichtschlag
**Supervision:** Anna Lichtschlag, Bramley J. Murton
**Validation:** Anna Lichtschlag
**Writing – original draft:** Adeline Marie Dutrieux, Anna Lichtschlag, Fernando J. A. S. Barriga, Sofia Martins, Jelena Milinovic, Bramley J. Murton
**Writing – review & editing:** Adeline Marie Dutrieux, Anna Lichtschlag, Fernando J. A. S. Barriga, Sofia Martins, Jelena Milinovic, Bramley J. Murton

in situ authigenic mineralization from low-temperature fluids, and the physical and chemical degradation of seafloor massive sulfide (SMS) structures. After formation, mass wasting can transport and redeposit hydrothermal materials either close to their origin or in more distal environments (German et al., 1993; Goulding et al., 1998; Hein et al., 2008; Webber et al., 2015).

Hydrothermal sediments are used as records of the spatial distribution, intensity, evolution and history of hydrothermal activity (Gurvich, 2006) and are suggested to be good indicators for the presence of hydrothermally active, extinct and buried sulfide bodies (Liao et al., 2018). It has been suggested that hydrothermal sediments themselves may present a resource potential, for example, the Atlantis II Deep in the Red Sea is estimated to contain ~90 Mt of hydrothermal metalliferous sediments (Bertram et al., 2011). Where preserved, they constitute a significant but hitherto unaccounted for reservoir of base and ferrous metals that are ultimately supplied to subduction zones, where they are recycled either back into the mantle or to the surface via arc volcanism. Hence, hydrothermal sediments probably play an important role in global metal cycles and budgets.

After deposition, hydrothermal sediments can undergo further modifications through weathering, ingress of oxygenated seawater and diagenesis. These processes lead to dissolution and leaching of minerals, metal remobilization, remineralization, reprecipitation, and/or loss to the water column. Hence, when using these sediments as indicators of hydrothermal activity, as vectors to locate hydrothermal deposits, for history reconstruction, and to assess their resource potential, we need to understand what controls their distribution across hydrothermal fields, the role of specific physicochemical environments of deposition, and the effects of weathering and diagenesis on their preservation and metal tenor.

The Trans-Atlantic Geotraverse Hydrothermal Field (TAGHF) is one of the best-known hydrothermal fields and is considered a classic example of a modern seafloor volcanogenic massive sulfide deposit, that is, having a typical surficial lens of massive sulfides and a deeper stockwork (Hannington et al., 1998). Metal-rich sediments are widely distributed in the TAGHF (e.g., M. R. Scott et al., 1978) and are often capped by biogenic calcareous ooze, which is also rich in Fe and Mn oxyhydroxides and sulfide particulates derived from hydrothermal plume fall-out (German et al., 1993; Mills et al., 1993; Shearme et al., 1983).

Here, we examine the controls on the deposition and preservation of hydrothermal sediments at the TAGHF, especially their base metal content and distribution. We explore how their formation and preservation varies in different physicochemical environments, that is, at the top of extinct hydrothermal SMS mounds, the slope and base of these mounds, and in more distal depositional channels and basins. Using a series of gravity cores, we compare sediments sampled from these different environments, focusing on their metal contents, mineralogy, modes of deposition, metal concentration, diagenesis, mobilization, and preservation.

## 2. Geological Setting

The TAGHF is located on the hanging wall of a west-dipping active detachment fault on the eastern flank of the Mid-Atlantic Ridge (26°09.4′N, 44°49.0′W) at a water depth of 3,600 m (deMartin et al., 2007). It comprises (Figure 1): (a) the hydrothermally active high-temperature TAG mound, (b) a zone of low temperature diffuse flow, and (c) two major areas of hydrothermally extinct sulfide mounds (i.e., the Alvin zone and the Mir zone; Dilek et al., 2000; Humphris & Tivey, 2000). The active TAG mound is a black smoker complex with chimneys at the summit, covered in sulfide talus and manganese crusts. The extinct Alvin zone contains several sulfide mounds, that is, Shinkai mound, Southern mound, Double mound and Rona mound (Petersen & Scientific Party, 2016; Rona, Hannington, et al., 1993; White et al., 1998) with discontinuous sulfide outcrops, standing and toppled chimneys, and a thin (<0.5 m) layer of pelagic carbonate ooze (Rona, Bogdanov, et al., 1993; Rona, Hannington, et al., 1993). The second inactive area, the Mir zone, consists of a broad area of small hydrothermally inactive sulfide chimneys, both standing and fallen onto the seafloor, covered in highly weathered sulfide material, red iron oxide-rich sediments and low-temperature hydrothermal precipitates such as Fe-Mn oxide crusts (Rona, Bogdanov, et al., 1993; White et al., 1998).

## 3. Materials and Methods

### 3.1. Sediment and Porewater Sampling

Sediment cores from three different geomorphological environments (Figure 1), identified from high-resolution bathymetry (Petersen & Scientific Party, 2016), were collected with a gravity corer (GC) during RRS James

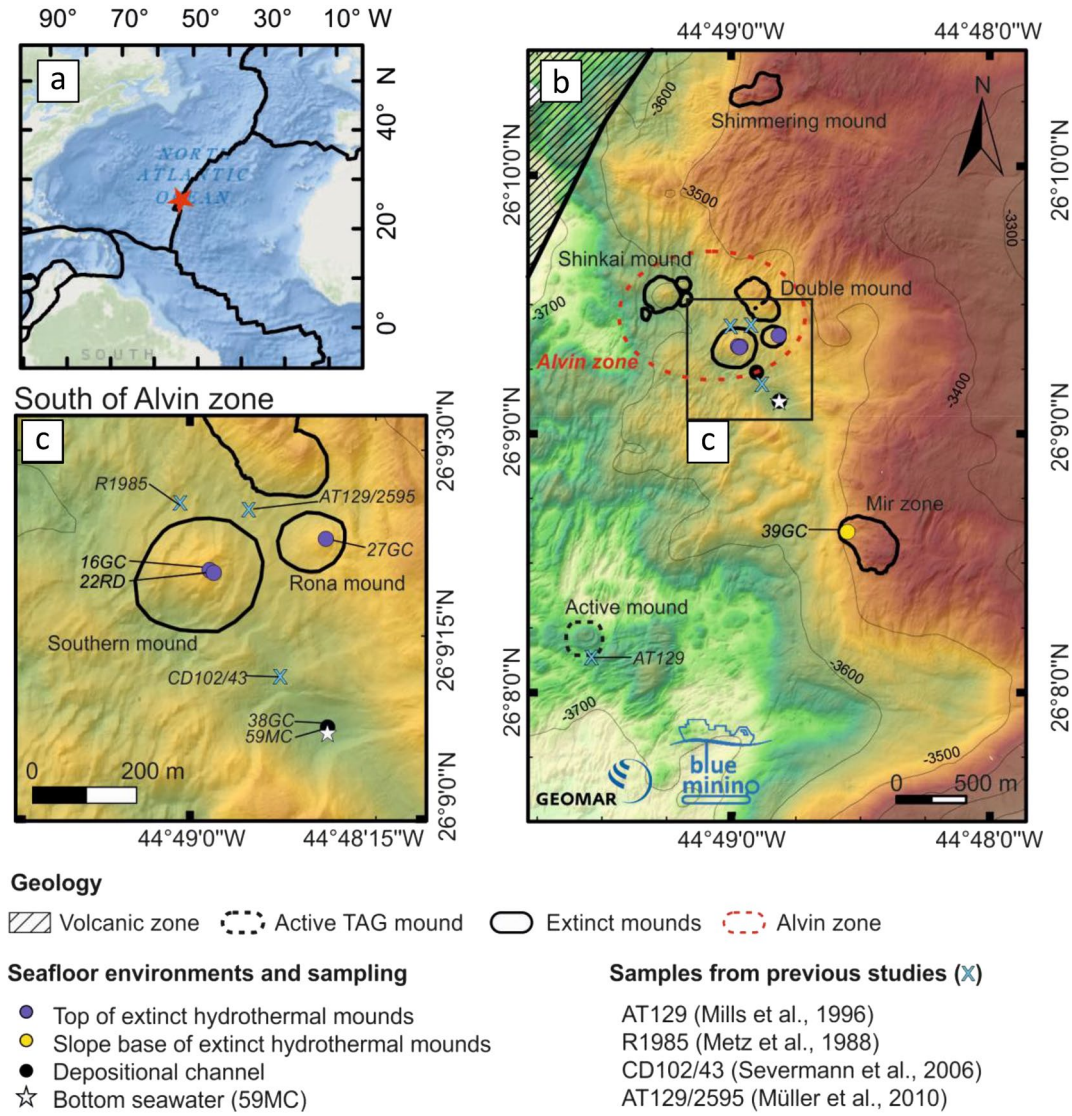


**Figure 1.** (a) Location of the Trans-Atlantic Geotraverse hydrothermal field (TAGHF) (red star) on the Mid-Atlantic Ridge (base map from GEBCO-ESRI); (b) Shaded bathymetry map with main hydrothermal sites of the TAGHF (Petersen, 2019; Petersen & Scientific Party, 2016). The active TAG mound, the four extinct mounds grouped into the Alvin zone, the Mir zone and the low-temperature active Shimmering mound are circled in black; (c) Zoom-in on the south of the Alvin zone with Southern and Rona mounds and the depositional channel with coring and drilling locations from this study and previous studies.

Cook cruise JC138 in 2016 (Table 1). The environments were (a) the tops of distinct hydrothermally inactive SMS mounds (i.e., Southern mound and Rona mound; 16 and 27GC); (b) a sedimentary fan covering the lower slope of the Mir zone (39GC), and (c) a depositional channel located in the south of the Alvin zone and several hundreds of meters distant from any known SMS deposit (38GC; Figures 1b and 1c). An additional sediment core was recovered from above the massive sulfide ore body beneath the top of the Southern mound using the seafloor rock drill RD2 (22RD). Near-bottom water was sampled from above hydrothermal sediments collected with a mega corer (59MC) in the depositional channel (Figure 1c).

After retrieval, porewaters were extracted from sediment cores through holes drilled in the plastic core liners and Rhizon filters inserted and connected to air-tight syringes (Lichtschlag et al., 2015; Seeberg-Elverfeldt et al., 2005). Sampling intervals were 5 cm in the first 50 cm (or when changes in lithology were visible) and 10 cm below 50 cm. Porewater sub-samples were acidified with 5 µL of concentrated $HNO_3$ (68%) for analyses of cations, preserved in 2% zinc acetate for analyses of chloride, sulfate and dissolved hydrogen sulfide, stored

headspace-free in 2 mL glass vials and fixed with saturated $HgCl_2$ for total alkalinity (TA) analysis, and frozen at −20°C for $NO_x^-$ ($NO_2^- + NO_3^-$) and $NH_4^+$ analysis. After porewater extraction, the sediment cores were split horizontally, described and logged for lithology and texture. Sediment subsamples were taken from the undisturbed sediments adjacent to the porewater samples and used for analyses of grain size, mineralogy and bulk rock geochemistry. All presented results are available in the Pangaea data base (https://doi.pangaea.de/10.1594/PANGAEA.922078) or Supporting Information S1.

### 3.2. Solid Phase Analyzes

Particle sizes of sediments were measured on selected samples with a Malvern Masterize particle size analyzer. X-ray diffraction qualitative analyses were carried out on powdered sediments with a Philips X'Pert pro with a Cu tube (K$\alpha$1 $\lambda$ = 1.541 Å) and Siroquant XRD software and on a PANalytical X'PERT Pro, a MiniFlex II, and X'Pert High Score Plus software (Milinovic et al., 2020) and results are presented in Table S3 of Supporting Information S1. A few milligrams of powder from selected samples were analyzed by scanning electron microscopy (Leo 1450VP SEM), and characterized by semi-quantitative energy dispersive X-ray (EDS) analyses with a carbon coating. Minerals that did not dissolve during the acid digestion were analyzed with a tabletop SEM (Hitachi TM1000).

The chemostratigraphy of the sediments was analyzed in a 1 mm vertical resolution with the ITRAX core-scanning X-ray fluorescence system (Cox Analytical Systems; Croudace et al., 2006) at the British Ocean Sediment Core Research Facility (BOSCORF) in Southampton, UK. The instrument was operated at a voltage of 30 kV, a current of 30 mA, and a count time of 30 s with a 3 kW Mo X-ray tube. Element abundances were normalized to kilocounts per second (kcps) and a running average of 5 mm was applied to the results.

Whole-rock analyses were performed by inductively coupled plasma mass-spectrometry (ICP-MS; ThermoScientific X-Series 2) for minor and trace elements, including rare earth elements (REE) and inductively coupled plasma optical emission spectrometry (ICP-OES; Thermo Scientific ICAP 6500 Duo) for major elements on approximately 100 mg of acid-digested, dried material. After oxidation of sulfides and carbonates in aqua regia, the mixture was digested using a mixture of HF and $HClO_4$ to dissolve any remaining silicates. The samples were diluted with 3 mol/L HCl and 3% $HNO_3$, containing an internal spike of Be, Re and In. Precision and accuracy were determined for each analytical run by repeated analysis ($n$ = 3) of two certified reference materials (CRMs): (a) marine sediments MESS-1 (NRC Canada), and (b) sulfide ore mill tailings RTS-1 (NRC Canada). Averages for each run were found to be less than 4% (precision) and 3% (accuracy), except for Co and Zn which had accuracy of 7% and Ba which had an accuracy of 15% (Tables S1.1 and S1.2 in Supporting Information S1). Limits of detection (LOD) for ICP-MS and ICP-OES analyses can be found in Table S1.3 of Supporting Information S1. The REE precision and accuracy were both within 5% of the CRM MESS-1. REE data were normalized to C1 chondrites (Evensen et al., 1978).

### 3.3. Porewater Analysis

Concentrations of dissolved major cations ($B^+$, $K^+$, $Mg^{2+}$, $Na^{2+}$, $Rb^{2+}$, and $Sr^{2+}$) were measured with ICP-OES and concentrations of dissolved minor cations ($Ba^{2+}$, $Co^{2+}$, $Cu^{2+}$, $Fe^{2+}$, $Mn^{2+}$, and $Zn^{2+}$) were measured with ICP-MS on aliquots that were 50-fold diluted with 3% thermally distilled $HNO_3$ containing an internal spike of Be, Re and In. Precision and accuracy of the measurements were determined with CRMs: (a) CRM-SW (Seawater Greyhound) and (b) SLEW-2 (NRC Canada) spiked with $Fe^{2+}$, $Mn^{2+}$, $Cu^{2+}$, $Zn^{2+}$, and $Co^{2+}$. Precision was better than 3% for all elements, and accuracy varied between 1.6% and 14.3% (Table S2.1 in Supporting Information S1). Limits of detection can be found in Table S2.2 of Supporting Information S1. Chloride and sulfate concentrations were analyzed by ion exchange chromatography using a Dionex ICS2500 with 9 mmol/L $Na_2CO_3$ as eluent on 100-fold diluted samples. The reproducibility of the results was determined using the International Association for the Physical Sciences of the Oceans (IAPSO) seawater standard. Precision was better than 1% and accuracy was better than 3.5%. Total dissolved hydrogen sulfide was determined using the method of Cline (1969). TA was determined using titration against 0.01 mol/L HCl using a mixture of methyl red and methylene blue as indicators. Analyses were calibrated against the IAPSO seawater standard. Precision and accuracy were better than 8% and 2%, respectively. $NO_3^-$ and $NH_4^+$ were measured using an AA3 Seal Analytics Autoanalyzer after Grasshoff et al. (1983); accuracy and precision of $NO_3^-$ calculated from the seawater nutrients CRM Lot.CA (www.kanso.co.jp/) was 8%.

## 4. Results

### 4.1. Sediment Distribution, Stratigraphy, and Mineralogy

We find a systematic variation in the mineralogy, lithology, stratigraphy and thickness of the hydrothermal sediments, depending on the different seafloor environments. These can be generalized into three types of environments depending on the proximity to the sources at the tops of the hydrothermal mounds.

1. Proximal sediments, found on top of extinct mounds, contain 4 units overlying a thick layer of jasper (amorphous iron-rich silica) that separates the sediments from massive sulfides below (Murton et al., 2019). Red to orange-colored, poorly sorted sedimentary units lying immediately above the jasper (forming Units 3 and 4, Figure 2) are mainly composed of goethite, hematite, nontronite, montmorillonite, quartz and amorphous Fe oxyhydroxides. Unit 3 contains some grains (up to 2 mm) and mm- to cm-size agglomerates and some larger individual clasts of Fe oxyhydroxides. On the Southern mound, Unit 3 also has some intervals containing coarse-grained detrital barite crystals with slightly eroded but delicate rosette-shaped crystal habits (Figure 3a) of 0.3–1 mm in size (e.g., in 22RD at ~220 cm and 16GC at ~50 cm). These crystal morphologies are typical for primary barite found in hydrothermal chimneys that has precipitated from Ba-enriched hydrothermal fluids reacting with sulfate from seawater (Griffith & Paytan, 2012). Their presence as detrital grains in the sediments indicates an origin from hydrothermal chimneys, with the primary sulfides having completely dissolved and replaced by oxides. Unit 3 transitions into a heterogeneous, coarse and unsorted dark unit (Unit 2), composed of heterogeneous brecciated material containing Fe and Mn oxides (todorokite, birnessite). The layer closest to the sediment surface (Unit 1) is composed of beige pelagic ooze (Figure 2a, Figure S1 in Supporting Information S1), consisting of calcareous foraminifera and other nanoplankton and iron oxide particles including goethite and amorphous ferrihydrite. Sediments from the tops of the extinct hydrothermal mounds (Southern and Rona mounds) are devoid of sulfide grains, but visual observations of the seafloor identified dark patches of ferromanganese crusts and some relict sulfide chimneys and boulders on top of the mounds confirming their hydrothermal origin. The rocks on top of the mounds are generally encrusted with secondary minerals, that is, red iron oxyhydroxides, yellow jarosite, or green atacamite/paratacamite.
2. Medial distant sediments, found at the base of the extinct mounds (e.g., the Mir zone fan, 39GC) consist of fine-grained Fe oxyhydroxides (Unit 5, goethite and ferrihydrite) and sandy layers of sulfides (Unit 6; mainly pyrite and chalcopyrite), but without calcite or detrital aluminosilicates. While grains of pyrite show euhedral crystal facets, chalcopyrite has a vuggy texture associated with partial dissolution (Figures 3b and 3c). The surface pelagic sediment layer is thinner (<0.5 m) than that at the top of the mounds, and observations of the seafloor show frequent boulders of massive and chimney sulfide material. Similar to those from the top of extinct mounds, these rocks are encrusted with secondary minerals, for example, oxyhydroxides, jarosite, and atacamite/paratacamite. The surface sediments at the base of the Mir zone are composed of up to 39 cm of sandy metalliferous sediments that are devoid of any carbonates (Figure 2d).
3. Distal sediments, found in basins and depositional channels some distance from the hydrothermal mounds, are often exposed in fault scarps where they are at least 10 m thick and consist of an alteration of pelagic sediments with plume fall out and turbidites (Unit 7, 8). The stratigraphy shows differences in graded bedding (Figures 2a and 2b), typical of turbidite Bouma sequences (Bouma, 1962). These turbidities have an eroded base composed of sulfide grains mixed with sand-size oxide fragments (Ta), indicating a high energy flow, with grain-size fining upward followed by the sequences Tb, Tc, and Td with fine dark brown sand and silt grains (Figure 2f). The uppermost sequence (Te) is composed of clay. The fining-upward sequences are mainly composed of Fe oxyhydroxides (hematite, nontronite, goethite, ferrihydrite) with sub-hedral cubic pyrite, sphalerite (with chalcopyrite disease), and chalcopyrite at the base of the turbidite sequence Ta (Figure 3d). Chalcopyrite disease (Bortnikov et al., 1991) is present as fine chalcopyrite intergrowths or disseminations in sphalerite that may result from replacement or co-precipitation in the presence of high-temperature Cu-rich fluids and is typical for seafloor and volcanogenic massive sulfide deposits. The upper Bouma sequences (Td, Te; Bouma, 1962) are often eroded and show a return to pelagic sedimentation conditions that may not have always been preserved between subsequent turbidity flows.

### 4.2. Geochemistry

Representative geochemical results for each depositional environment are shown in Figures 4 and 6 (i.e., 16, 39, and 38GC; additional data from 27GC in Table S4 and Figure S2 in Supporting Information S1). When the uppermost sediment layer, for example, Unit 1 on the top of the mound, is present, it is dominated by carbonate

10.1029/2023GC010879

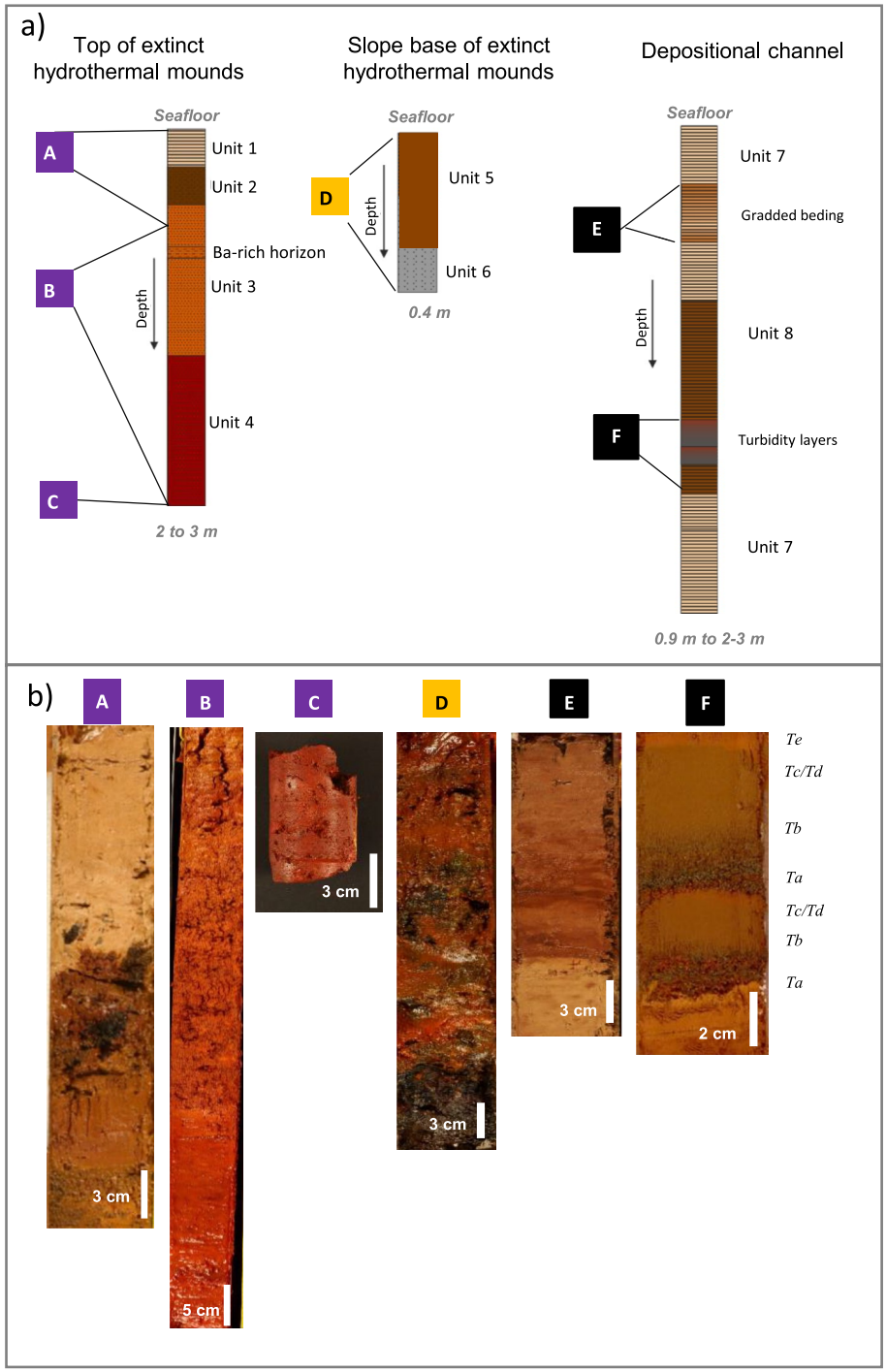


**Figure 2.** Schematic stratigraphy logs (upper panel a) and exemplary photographs (lower panel b) of selected hydrothermal sediments cores from the Trans-Atlantic Geotraverse hydrothermal field. (A) Carbonate ooze cap (Unit1) followed by dark Mn oxide crusts at Rona mound (Unit 2, 27GC). (B) Transition between Unit 3 and Unit 4 on the top of Southern mound (22RD). (C) Silicified Fe-rich "jasper" directly below the sediment cover and above the sulfide ore body. (D) Mir zone fan sediments, showing numerous sulfide grains and pebbles mixed with Fe oxyhydroxides (39GC); Unit 5: oxyhydroxides formed from transported material; Unit 6: sulfide sands. (E) Layering due to the settling of plume fall-out particles within the pelagic carbonate ooze and (F) turbidity flow layers showing a Bouma sequence (38GC); Unit 7: pelagic sediments with different levels of plume fallout and turbidities; Unit 8: turbidity flows.

10.1029/2023GC010879

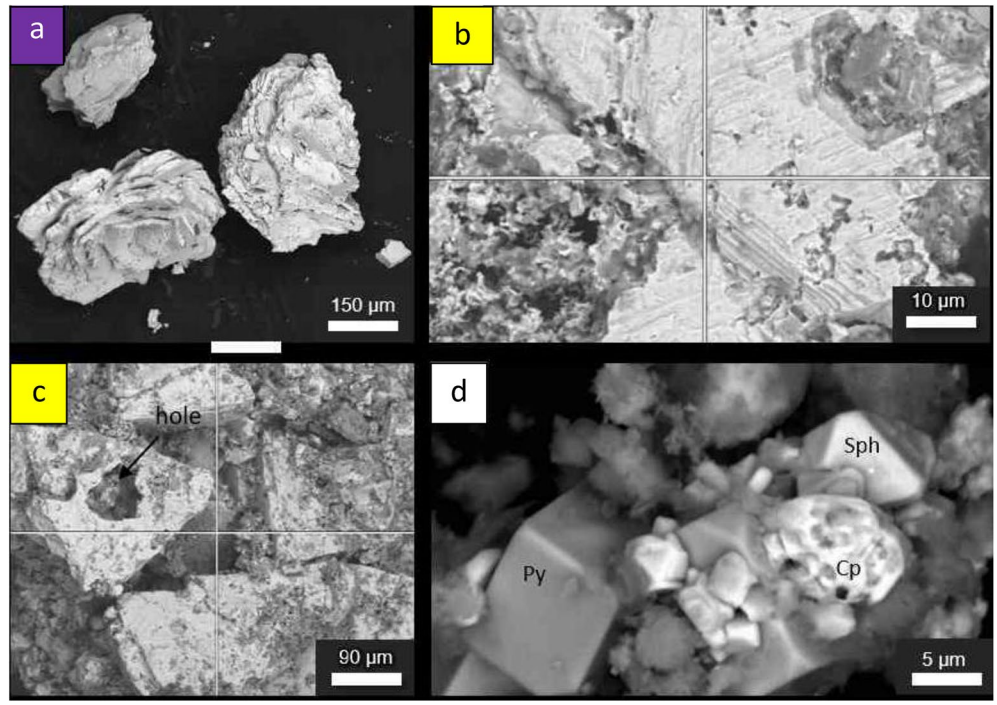


**Figure 3.** SEM microphotography. (a) Detrital barite grain from Unit M3 of Southern mound (22RD, 150 cm depth); (b) Zoom-in onto the chalcopyrite dissolution pitting; (c) few hundred µm long chalcopyrite grains with indications of partial dissolution pitting from the Mir Zone fan (d) few tens of µm long aggregate of fine grained cubic pyrite (Py), partially dissolved chalcopyrite (Cp) and Cu-rich sphalerite (Sph) presenting octahedron faces and likely chalcopyrite disease (Barton & Bethke, 1987) from a thin sulfide layer in the depositional channel.

**Table 1**
*Locations and Station Positions of Gravity Cores (GC), the Mega Core and the Rock Drill Core (RD) at the Trans-Atlantic Geotraverse Hydrothermal Field, Including the Analyses From Each Core That is Presented in This Study*

| Core reference | Location | Core length (cm) | Water depth (m) | Coordinates | Analyses |
|---|---|---|---|---|---|
| Top of extinct hydrothermal mounds | | | | | |
| 16GC | Southern mound | 133 | 3,510 | 26°09′20″N 44°48′68″W | Porewater and solid phase composition, XRD |
| 22RD | Southern mound | 190–320[a] | 3,535 | 26°09′20″N 44°48′57″W | SEM, XRD, REE solid phase composition |
| 27GC | Rona mound | 41 | 3,524 | 26°09′23″N 44°48′49″W | Solid phase composition (Figure S2 in Supporting Information S1), XRD |
| Slope base of extinct hydrothermal mounds | | | | | |
| 39GC | Mir zone fan | 39 | 3,490 | 26°08′37″N 44°48′33″W | Porewater and solid phase composition, SEM |
| Depositional channel | | | | | |
| 38GC | 500 m SE of Southern mound | 98 | 3,608 | 26°09′7″N 44°48′49″W | Porewater and solid phase composition, SEM |
| 59MC | 500 m SE of Southern mound | 15 | 3,528 | 26°09′7″N 44°48′49″W | Seawater composition (Table S5 in Supporting Information S1) |

[a]Depth below the seafloor for the drill core is inferred from RD2 drilling telemetry data.

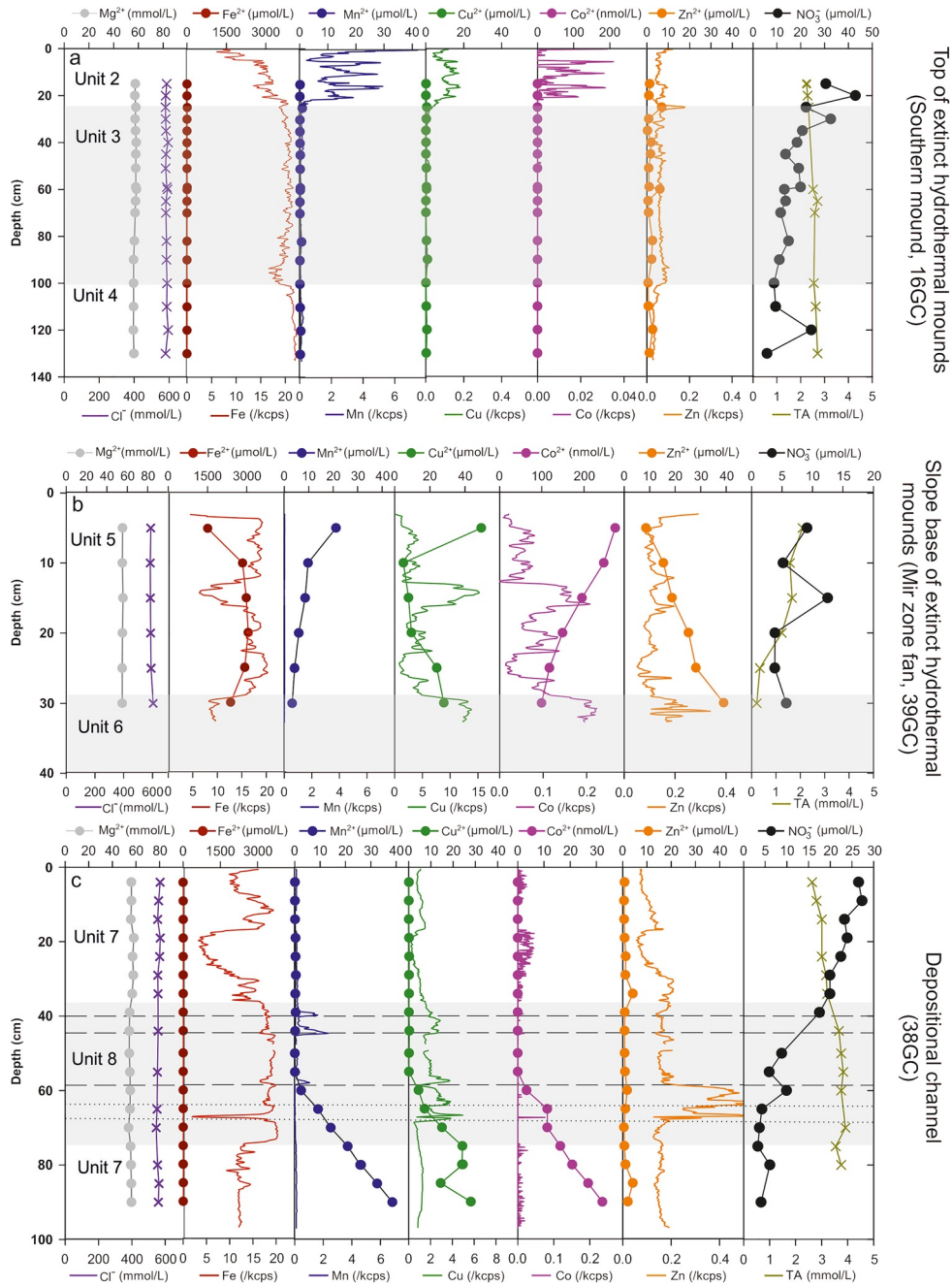


**Figure 4.** Down-core profiles of chemostratigraphy (solid lines) and solid phase metal contents in selected cores from the three different environments: (a) proximal: on the top of an extinct mound (Southern mound, 16GC); Unit 1 was not recovered for 16GC and its chemostratigraphy and solid phase content is displayed in Figure S2 of Supporting Information S1 (27GC); (b) medial distant: at the base of a slope (Mir Zone fan, 39GC); (c) distal: in the depositional channel (38GC). Note the different scales of Cu and of Co in the different panels. Shaded depths correspond to the lithology units in text and Figure 3. Dashed lines in (c) correspond to Mn-rich layers and the dotted lines correspond to sulfide layers. Photographs of the cores are displayed in Figure S1 of Supporting Information S1.

ooze that contains an average of 25 wt% Ca and up to 8.5 wt% Fe (27GC) in a bimodal mixture ($R = -0.98$). Other metals present in this ooze include Mn (0.19–0.31 wt%; mean 0.25 wt%), Cu (0.09–0.14 wt%; mean 0.12 wt%), Zn (0.03–0.08 wt%; mean 0.06 wt%), and Co (18–21 ppm; mean 20 ppm).

1. On top of the mounds, the deepest sediment units (Unit 3, Unit 4) have low to negligible mean contents of trace metals (Cu 0.05 wt%, Zn 0.16 wt%, Co < 1.27 ppm and Mn 0.14 wt%). In contrast, horizons with

maximum Mn enrichment are found in Unit 2 (Figure 4a), for example, with 16 wt% Mn at Southern mound (16GC), and 20 wt% Mn at Rona mound (27GC, Figure S2 in Supporting Information S1). Unit 2 also shows increased and variable content in trace metals, for example, at Rona mound Unit 2 sediments are enriched in Cu (1.42 wt%), Zn (0.7 wt%), and Co (190 ppm). In Unit 2, Co correlates with Mn ($R = 0.67$, Table S6.2 in Supporting Information S1)

2. In the medial distant sediments at the base of the slope of the mounds (i.e., Mir zone fan, Figure 4b), contents of Cu, Co, Zn and S increase with the presence of sulfide minerals (e.g., pyrite and chalcopyrite at a depth interval of 30 cm, Unit 6). Statistical analyses show that Cu, Co and Zn are preferentially found in sulfide minerals ($R = 0.75$, 0.80, and 0.52, respectively, Table S6.4 in Supporting Information S1), rather than Fe-oxide phases (a strong negative correlation with $R = -0.88$, $-0.79$, and $-0.62$, respectively) or Mn-oxide phases (a strong negative correlation with $R = -0.91$, $-0.79$, and $-0.48$, respectively).
3. In the turbidite layers of the distal depositional channel (Unit 8 in Figure 4c), numerous sulfide mineral-rich horizons (i.e., at depths 58 64 and 68 cm, Figure 3d) are identified by peaks in S content and enrichments in Cu and Zn (up to 7.23 wt% and 0.88 wt%, $R = 0.56$ and 0.73, respectively, Tables S4 and S6.6 in Supporting Information S1). Mn is also enriched, but limited to three distinct horizons, that is, at 40 cm (1.66 wt%), 45 cm (0.85 wt%), and 57 cm (0.83 wt%) in which Cu and Co contents also increase up to 7,23 wt% and 214 ppm, respectively. In the shallower pelagic unit (Unit 7) above the turbidite layers (Unit 8), the Fe content is variable (up to 23 wt%) and is directly related to the presence of various iron-oxyhydroxide phases and inversely proportional to the Ca (i.e., carbonate) content ($R = -0.99$). Cu and Zn contents are also directly proportional to the Fe content ($R = 0.9$ and 0.6, respectively).

### 4.3. Rare Earth Elements (REE)

REE patterns of marine sediments can be used to show hydrothermal input and sediment-seawater interactions, with positive Eu anomalies usually inherited from hydrothermal fluids and negative Ce anomalies usually inherited from seawater interactions (e.g., Elderfield, 1988). TAGHF sediment REE are plotted against fluid REE patterns and previous studies from the TAGHF in Figure 5. Pelagic sediments containing elevated iron content, such as in the graded bedding of the depositional channel, have a positive Eu anomaly (Figure 5a). The REE pattern for the Mn-oxide rich unit, Unit 2, shows both a positive Eu and a negative Ce anomaly (Figure 5b). Units exclusively composed of Fe oxyhydroxides (Unit 3 and Unit 4) have similar REE patterns, with concentrations that range over an order of magnitude, but are in general lower than those in the Fe-rich pelagic sediment, and exhibit a weak negative Ce anomaly and strong positive Eu anomaly (Figure 5c). The lowest REE concentrations are found in sulfide clasts in sediments from the slope base of the mound (Mir zone fan) and have a positive Eu anomaly but do not show a Ce anomaly (Figure 5c). REE abundance increases from TAG mound "fresh" sulfides, followed by "fresh" sulfides recovered in 39GC in the Mir zone fan (positive Eu anomaly, no Ce anomaly) towards oxides collected with the sulfides (positive Eu anomaly, negative Ce anomaly) and finally oxyhydroxide layers collected from Unit 4 (positive Eu anomaly, negative Ce anomaly). The highest Eu anomaly was found in the deepest Unit 4 next to the Fe-rich silicified layer at the Southern mound.

### 4.4. Porewater Geochemistry

To test for active hydrothermal fluid flow in the sediments, dissolved $Mg^{2+}$, $Cl^-$ and $SO_4^{2-}$ concentrations were measured in porewaters. Porewaters from all three depositional environments exhibit constant concentrations of these components with depth and have values similar to the composition of seawater (collected from the overlying water of a multicorer core, i.e., 57 mmol/L $Mg^{2+}$, 594 mmol/L $Cl^-$, and 29 mmol/L $SO_4^{2-}$; Table S5 in Supporting Information S1).

To test for microbial carbon degradation or diagenetic changes (e.g., carbonate dissolution), the TA of the sediments was measured. Proximal sediments from the top of the mounds have TA similar to seawater (2.4 mmol/L, Figure 6a). In contrast, in the medial sediments at the slope base (e.g., Mir zone fan), TA decreases from 2 mmol/L toward 0 at 30 cm (Figure 6b). In the depositional channel, TA almost doubled in concentration with depth from bottom seawater values (2.4 mmol/L) at the surface to 4 mmol/L at a depth of 70 cm (Figure 6c).

Dissolved trace metals ($Fe^{2+}$, $Mn^{2+}$, $Zn^{2+}$, $Co^{2+}$, and $Cu^{2+}$) were analyzed to test for dissolution and mobilization of metals from the deposited sediments. Throughout the cores on the top of the mounds, trace metals have low

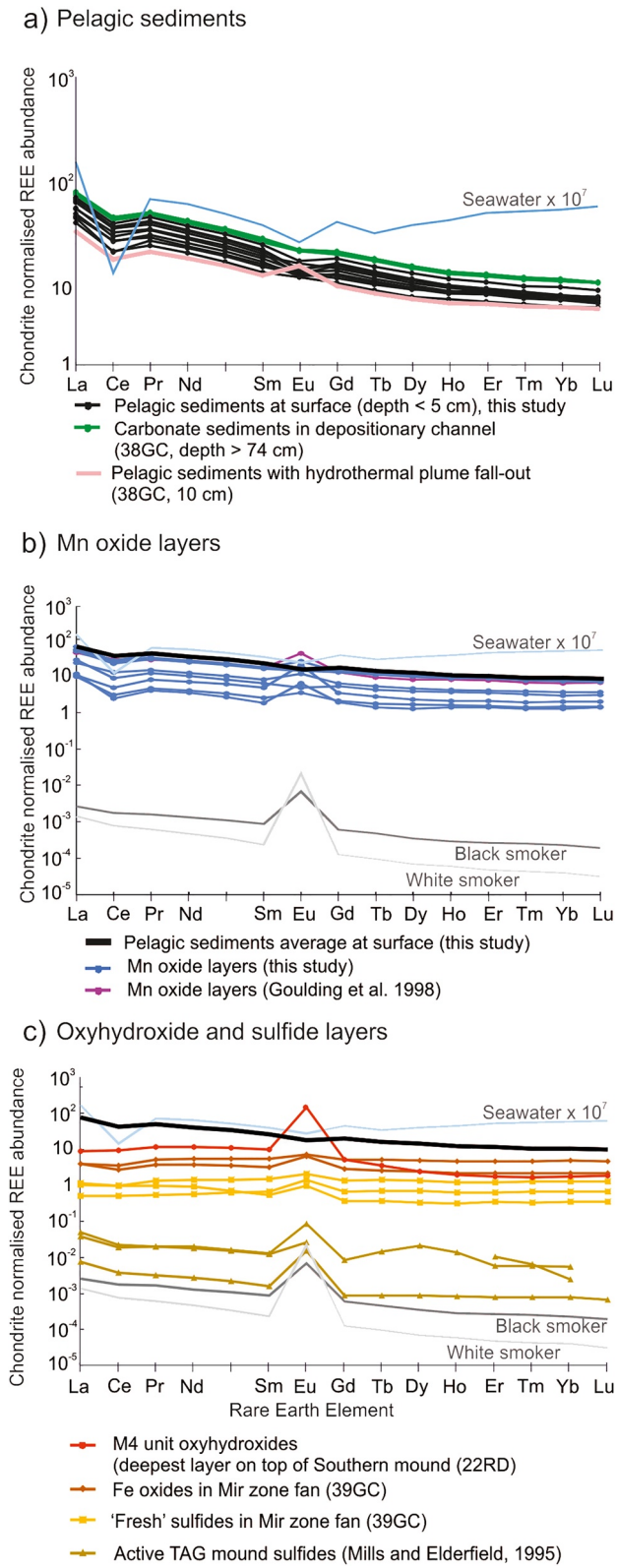


**Figure 5.**

concentrations with no distinctive trends (Figure 6a). In contrast, dissolved trace metal concentrations in sediments from the slope base of the mound (Mir zone fan) are between one and three orders of magnitude higher than in sediments from the top of the mounds or in the depositional channels. In general, Mn and $Co^{2+}$ increase toward the sediment surface, while $Zn^{2+}$ and $Cu^{2+}$ decrease, and $Fe^{2+}$ remains constant (Figure 6b). Maximal concentrations found are $Fe^{2+}$ (3,050 μmol/L), $Mn^{2+}$ (20 μmol/L), $Zn^{2+}$ (40 μmol/L), $Cu^{2+}$ (50 μmol/L), and $Co^{2+}$ (270 nmol/L). In the depositional channel (Figure 6c), $Fe^{2+}$ is low (mean of 2 μmol/L), and $Zn^{2+}$ variable with a maximum of 4 μmol/L. Below 60 cm depth, $Mn^{2+}$ and $Cu^{2+}$ concentrations increase with depth from <1 μmol/L up to 38 and 27 μmol/L, respectively, and $Co^{2+}$ increases from <0.1 nmol/L up to 32 nmol/L.

Concentrations of $NO_3^-$ decreasing with increasing sediment depth are an indicator of microbial activity (i.e., denitrification or nitrate reduction) and increasing $NH_4^+$ concentrations with depth also indicate the decomposition of organic matter. In the depositional channel (38GC), $NO_3^-$ has concentrations typical of the North Atlantic Deep Waters (Hansell & Follows, 2008) at the sediment surface, but is nearly absent (3 μmol/L) at 120 cm below the sea floor (Figure 6c). In the same core (38GC), $NH_4^+$ concentrations peak at 38 μmol/L at a depth of 25 cm. At the southern mound (16GC), the $NO_3^-$ concentrations also decrease from 43 μmol/L to 6 μmol/L (at a depth of 130 cm) (Figure 6a). In all cores, the dissolved sulfide concentration is below 2 μmol/L, which is close to the LOD (1 μmol/L).

## 5. Discussion

At the TAGHF, hydrothermal sediments are present in three distinct depositional environments: at the tops of hydrothermal mounds, their slopes and bases, and accumulated in distal channels and basins. Despite a common origin, that is, hydrothermal activity, we find distinct differences in the content and distribution of metals in these sediments. We suggest that these differences indicate different mechanisms for metal deposition, preservation and remobilization related to transport, depositional environment, weathering, and post-depositional diagenetic processes after burial.

### 5.1. Physical Transport as Controls of Metal Distribution

At the TAGHF, concentrations of many non-ferrous metals, including Cu, Zn and Co, are higher in the hydrothermal sediments at the base of the extinct mounds and in distal channels than in those on top of the hydrothermal mounds. For example, at the base of the mounds the average Cu content is almost 7 times higher (14.2 wt%) than in the depositional channel (2.2 wt%) and two orders of magnitude higher than on the mound tops (0.2 wt%). In the sediments at the base (e.g., Mir zone fan), sulfide grains are present and the metal content is similar to the massive sulfides exposed on top of the Mir zone mound (0–26.8 wt% Cu, 0–22 wt% Zn and 2.5–1,100 ppm Co (Hannington et al., 2004; Krasnov et al., 1995; Petersen, 2000; Rona, Hannington, et al., 1993), compared to 2–28 wt% Cu, 0.1–0.4 wt% Zn and 4–104 ppm Co in the sediments), providing a geochemical indicator for the provenance of those sediments from the disintegration of chimneys and massive sulfides. The cm-thick layers of unsorted sulfide sands at the base of the mounds, intermixed with fine-grained Fe oxyhydroxides, confirm a proximal type of sedimentary facies, typical of rapid deposition and short transport distances. The only partial alteration of the sulfide minerals shows that the material was transported downslope and rapidly buried, preventing full weathering. In addition, the absence of biogenic or detrital (i.e., non-hydrothermal) components further confirms rapid deposition compared to the background pelagic sedimentation (sedimentation rate of ∼8 cm/ka for sediments enriched in vent-derived particles, Metz et al., 1988). Rapid burial and short transport distances for proximal sediments are in agreement with previous studies that have shown that the degree of physical disintegration of sulfide minerals, the thickness of depositional beds, and the degree of grain-size sorting are directly proportional to the distance the material has been transported (Webber et al., 2015). Preservation of metals at the base of hydrothermal mounds has also been reported from active hydrothermal mounds, for example, unsorted sulfide-rich horizons are largely present in sediments recovered from around the active TAG mound (push-core AT129; Figure 1; Mills et al., 1996; Petersen, 2000). Similarly, at the Beebe Vent Field, Mid-Cayman Spreading

**Figure 5.** Chondrite-normalized rare earth element fractionation distribution; (a) Trans-Atlantic Geotraverse hydrothermal field (TAGHF) pelagic sediments from the surface, at depth and containing hydrothermal plume fall-out; (b) TAGHF Mn-rich layers and background sedimentation; (c) TAGHF sediment oxides and sulfides. Reference data for seawater (North-Atlantic Deep waters) scaled by $10^7$ from German et al. (1990) and Mitra et al. (1994); black smokers from Douville et al. (1999); white smokers from Mitra et al. (1994) and active TAG mound from Mills and Elderfield (1995) (note that Gd-Er and Lu for one of the sulfide samples (brown line) is not presented in the original publication).

10.1029/2023GC010879

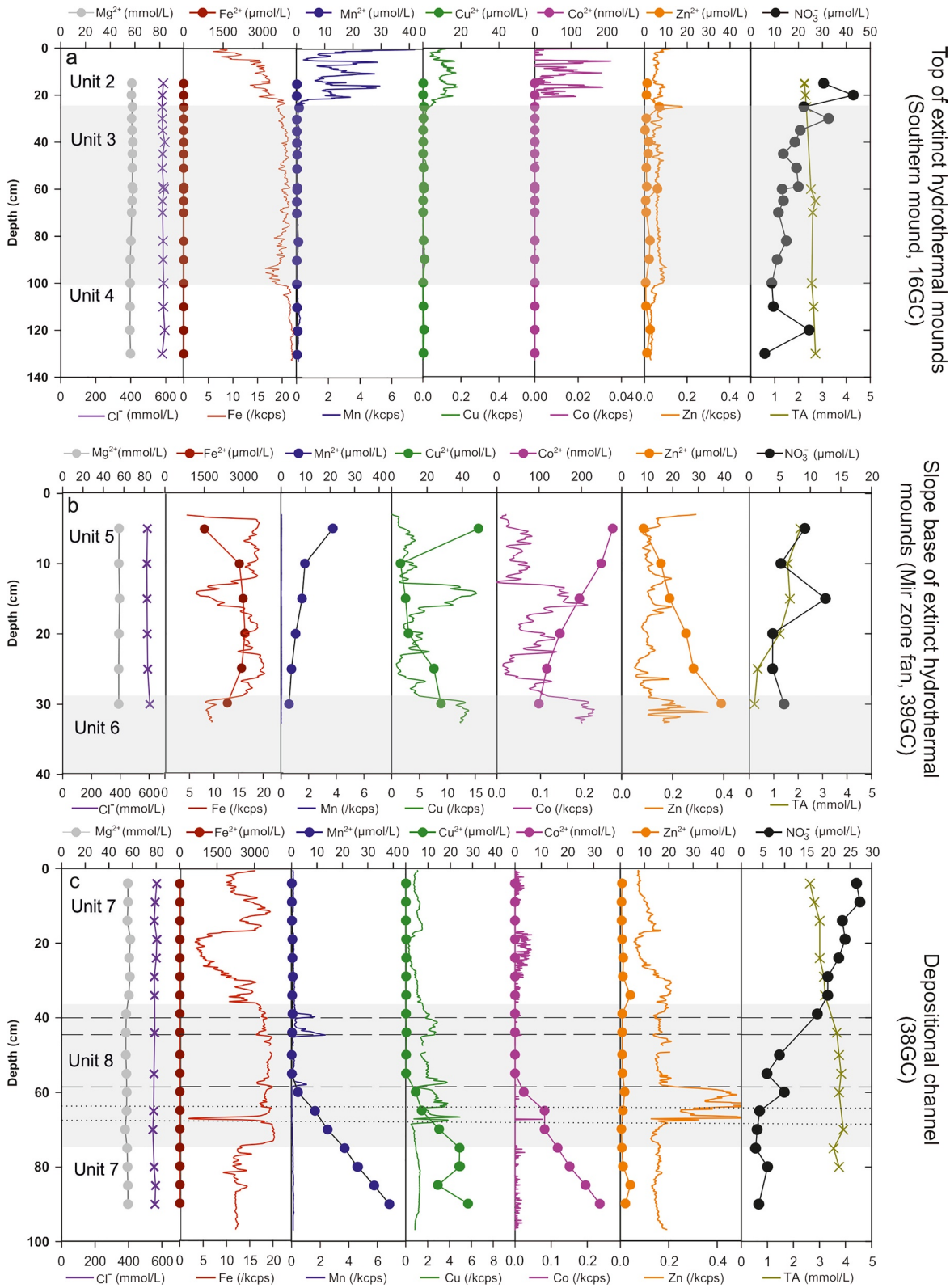


**Figure 6.**

Center, sediments rich in coarse-grained sulfides and fine-grained iron oxides have been recovered from seafloor depressions located within 100 m of the active mounds (Webber et al., 2015). The triggering mechanism of such mass wasting, rapid transport, and deposition events is most likely slope instability, induced by steep topography (e.g., rapid growth of hydrothermal chimneys), active tectonism (mid-ocean ridge seismicity), and/or high accumulation rates at the source (Shanmugam, 2018). Hence, the base of extinct SMS mounds is an environment where sulfide mineral-rich sediments with high metal contents can accumulate. It is probable that the physical transport and rapid burial of the material is the primary mechanism for metal distribution and preservation in these sediments.

Beyond the base of the extinct mounds, the transport mechanisms change, and hydrothermal material are transported by turbidity currents that eventually deposit sediments in distal ponds and channels hundreds of meters away from the mounds. This mode of transport and deposition is evident from the fining-upward sequences, with the basal layers formed from heavy sulfide sands that originated from hydrothermal structures (e.g., chimneys), and upper layers composed of finer clays and oxyhydroxide particles. The presence of some eroded basal layers and the absence of interbedded background pelagic carbonates indicate that metalliferous sediments are also here rapidly deposited. Transport of hydrothermal material by turbidity current is a common phenomenon as similar stratigraphic sequences have been described for example, from the volcanogenic massive sulfide deposits at Tharsis, Iberian Pyrite Belt (Barriga & Carvalho, 1983). At greater distances (i.e., 500 m from the SMS mounds (38GC)) the proportion of pelagic sediment increases and more often distinct calcareous layers are found in between thin metalliferous ones.

While at the base of the mounds the high metal tenor in the sediment was indicative of their origin, the determination of provenance is more complex further away from the mounds. To test if we can identify the source of the hydrothermal sediments from their metal content, we compared the geochemical compositions of the sediments to that of massive sulfides and Fe oxyhydroxides collected from the tops of adjacent SMS mounds. For provenance discrimination, Cu and Zn were chosen as Cu usually originates from chalcopyrite, which is comprised in high-temperature "black smoker" chimneys and Zn usually originates from sphalerite, which is often contained in lower-temperature "white smoker" chimneys (e.g., Webber et al., 2015) both present at the TAGHF. In the TAGHF depositional channel sediments, Cu and Zn contents (0.1–7.2 wt% Cu and 0.1–0.88 wt% Zn, 38GC) are higher than in sulfides recovered from the nearby Southern mound (Murton et al., 2019; Petersen, 2000). Hence either the sulfides recovered from Southern mound already have a composition altered by weathering (i.e., the primary metal tenor has been altered), or the channel sediments are composite and derived from several sources, for example, incorporating material from neighboring SMS deposits such as the Rona mound, which is richer in Zn and Cu (i.e., 0–10.9 wt% Cu and 0–8.4 wt% Zn, Table S7 in Supporting Information S1), probably reflecting the greater influence of lower-temperature Zn-rich "white-smokers" during the stage feeding the sediments (see Blue Mining geochemical analyses provided in Table S7 of Supporting Information S1). Alternatively, post-depositional metal redistribution could have changed the metal tenor of the sediments.

In addition to downslope transport, fine-grained particulate hydrothermal plume fallout adds to the metal content in TAGHF sediments. Plume-derived input is differentiated from weathered and oxidized hydrothermal sediments by comprising well-sorted clay size particles. In the more distal areas at the TAGHF, plume fallout is particularly visible in pelagic sediments (Figure 2), with up to 10 times increase in Fe concentration (Table S4 and Figure S2 in Supporting Information S1) compared to background pelagic carbonate, and is accompanied by a slightly positive Eu anomaly and negative Ce anomaly (Figure 5a) typical for hydrothermal particulate plume fall out (German et al., 1993; Mills & Elderfield, 1995). While the distribution of plume-derived metals in pelagic sediments depends on the distance from their source and on direction and velocity of currents, their contribution to the mass-wasted sediment layers is difficult to assess due to the overall high metal content through physical transport and metal redistribution. In summary, for more distal hydrothermal sediments, the presence of turbidite layers with an order of magnitude higher metal content than the metalliferous deposits on top of extinct mounds interlayered with pelagic horizons with some plume fallout seems to be typical; however, due to several sources feeding into the channels with different metal contents or weathering and metal remobilization, the provenance of these sediments might be difficult to determine.

**Figure 6.** Down-core porewater geochemistry profiles for $Mg^{2+}$, $Fe^{2+}$, $Mn^{2+}$, $Cu^{2+}$, $Co^{2+}$, $Zn^{2+}$, $NO_3^-$ (dots), $Cl^-$ (crosses), total alkalinity (crosses) in the three different environments: (a) On the top of an extinct mound (Southern mound, 16GC); (b) At the base of a slope (Mir Zone Fan, 39GC); (c) In the depositional channel (38GC). Note the different scales for $Cu^{2+}$, $Co^{2+}$, an $NO_3^-$. Sediment chemostratigraphy (results identical to Figure 4) is plotted to highlight the relationship between porewater and solid phase geochemistry. Shaded depths correspond to the lithology units in the text and Figure 2. Dashed lines in (c) correspond to Mn-rich layers and the dotted lines correspond to sulfide layers. Photographs of the cores are displayed in Figure S1 of Supporting Information S1 and explanations of unit can be found in Figure 2.

### 5.2. Post-Depositional Metal Redistribution

To determine the fate of the metals in metalliferous sediments and their role in the local and global metal cycles, it is important to understand the processes they undergo after deposition. The lowest base-metal contents of all studied environments are found at the mound-tops at greater than 20 cm below the seafloor (Units 3 and 4), while the contents especially of Mn, Co, and Co are higher in the sediment layer above these units (Unit 2, Figure 4). Despite the low metal content, the geochemical and textural evidence suggests that the metalliferous sediments buried on top of the mounds originate from weathering of sulfides, that in turn are derived from the collapse of high-temperature hydrothermal sulfide chimneys. A hydrothermal origin is suggested from the positive Eu anomaly of the Fe-oxyhydroxide layers (Figure 5c), that is usually inherited from high-temperature hydrothermal fluids (Klinkhammer et al., 1994; Mills & Elderfield, 1995). Detrital barite crystals are also present in the sediments that are typically formed in high-temperature hydrothermal chimneys (Griffith & Paytan, 2012) (Figure 3a). The sediment textures include agglomerations of oxidized material that were originally fragments of sulfide debris, and the sediment is poorly sorted. In addition, visual surveys of the mound-tops showed that outcrops and relict chimneys of sulfides are present and it has been concluded that they are likely to contribute to the metalliferous sediments as they decay (Rona, Hannington, et al., 1993). Hence, despite a lower abundance of non-ferrous metals in the mound top sediments compared to other TAGHF environments, and the absence of sulfide minerals, the evidence suggests that the metalliferous sediments on top of the mounds represent completely weathered sulfides derived from the collapse of the high-temperature hydrothermal materials. With time, Cu and Zn were mobilized and leached and iron sulfides were replaced by insoluble iron oxyhydroxides, leading to an overall depletion of non-ferrous metals closest to their source, compared to the metalliferous sediments preserved by rapid burial in the other environments across the TAGHF (Figure 7a). Similar to the mound top sediments, initially, gossans have a high porosity and permeability due to the agglomeration of coarse particles (Goulding et al., 1998), so that seawater can circulate through the sediments, resulting in pervasive oxidative weathering.

In the top 20 cm of the mound top sediments (i.e., Southern mound) or just below the pelagic sediment cover (i.e., Rona mound), the metal content is slightly higher and Mn enrichment coincides with increased Co and Cu contents. This enrichment can either originate from re-precipitation of metals remobilized from deeper layers or from low-temperature hydrothermal fluids that percolated through the sediments after the high-temperature flow had ceased. Using a discrimination schema for oceanic Fe-Mn deposits (Josso et al., 2017), the metal content together with the REE distribution points toward low-temperature hydrothermal circulation as a source for the metal tenor. Across the TAGHF, the presence of ferromanganese crusts has been reported from the surface of the seafloor (R. B. Scott et al., 1974) and close to the active TAG mounds, and it is suggested that they have formed by ascending, chemically reduced, low-temperature hydrothermal fluids (Mills et al., 1996; Thompson et al., 1985). One interpretation of our results could be that also in the now extinct mound tops, low-temperature hydrothermal fluids might have percolated through the sediments. Dissolved metals might have been transported upwards under reduced conditions followed by redox-related precipitation, forming a metal-richer layer above a metal depleted layer. However, as present-day porewaters have seawater composition and dissolved $Mn^{2+}$ and other dissolved metals are absent, any metal remobilization and low-temperature fluid flow will have since ceased.

In contrast, more distal depositional environments, that is, at the base of the mounds, contain thick accumulations of sulfide-rich sediments with high concentrations and distinct gradients of dissolved metals ($Fe^{2+}$, $Mn^{2+}$, $Cu^{2+}$, $Co^{2+}$, and $Zn^{2+}$) in their porewaters. As these dissolved metal profiles in porewaters vary independently of the solid phase contents (Figure 6b) except for $Mn^{2+}$ that has very low solid phase concentrations, this indicates that these metals are currently dissolved and being mobilized in a way that is not correlated with or limited by solid phase availability. For example, different behaviors of dissolved metals are observed in porewaters, that is, $Zn^{2+}$ and $Cu^{2+}$ increase toward the sulfide-rich layer at 30 cm depth, $Co^{2+}$ and $Mn^{2+}$ decrease with increasing depth, and $Fe^{2+}$ concentrations remain constantly very high. High dissolved iron and manganese concentrations in sediments could be the result of microbial degradation of organic matter with iron and manganese oxides. However, although evidence for microbial degradation has been found in sediments elsewhere in the TAGHF (Figure 1; Glynn et al., 2006; Müller et al., 2010; Severmann et al., 2006), organic carbon content in TAGHF sediments has been shown to be relatively low (0.14–0.45 wt.%; Severmann et al., 2006) and only little pelagic sediment, supplying organic carbon through sedimentation, is present. Instead, there are indications of dissolution of sulfides in the sulfide-rich layer present at >30 cm depth. Weathering of sulfides is an acid-producing process that is accompanied by the release of metals. Although pH as an indicator for sulfide oxidation was not measured, low pH is consistent with the decreased TA values (close to 0) found

10.1029/2023GC010879

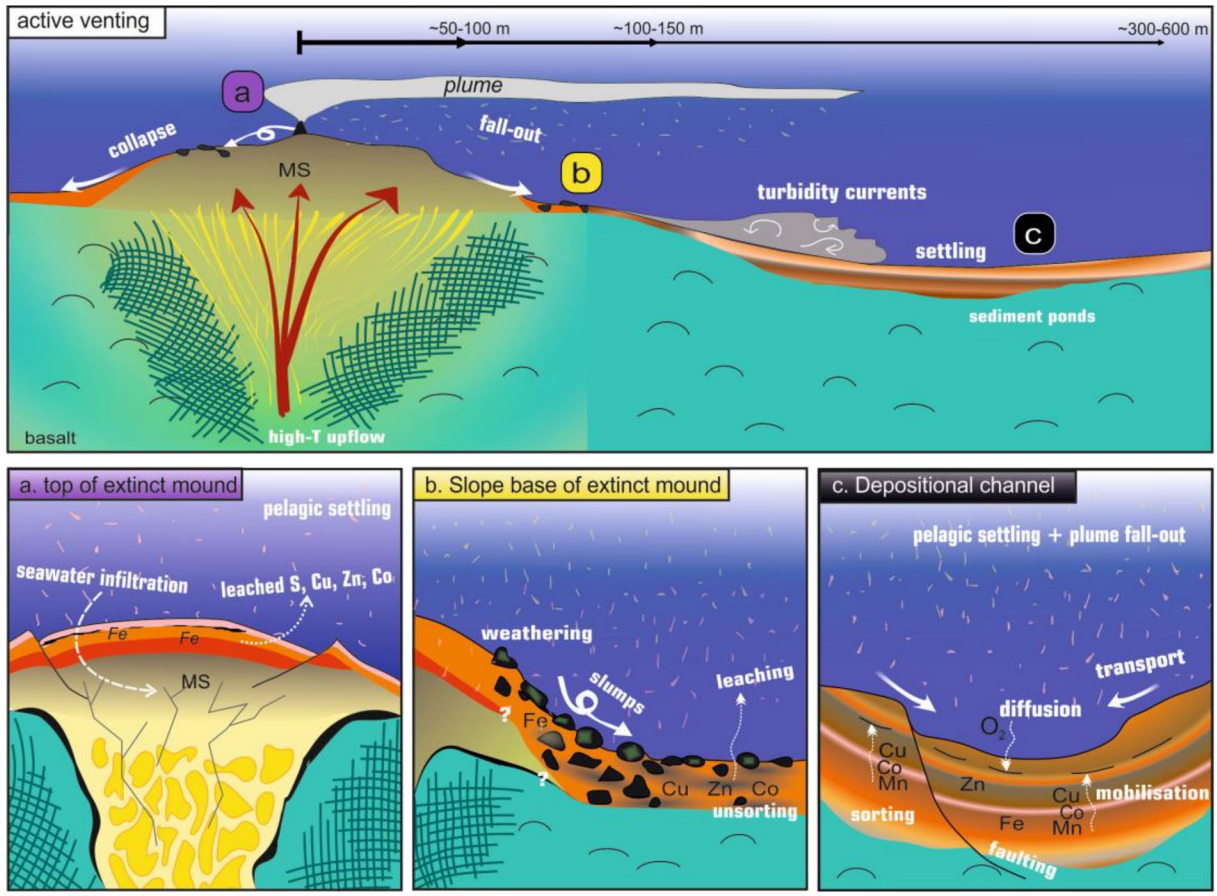


| | | | |
|---|---|---|---|
| **Sulfides** | Absent | Thick (cm) and assorted layers | Thin (mm) and sorted into turbidity *Ta* layer |
| **Fe** | Highest concentration as oxyhydroxides | Present | Present in turbitidy layers and in plume fall-out layers |
| **Mn** | Enrichment in discrete horizons as MnO2 crusts | Absent | Enrichment in discrete horizons |
| **Cu, Zn, Co** | Depletion except in Mn oxide horizons | Enrichment associated with sulfides | Enrichment associated with sulfides and Mn oxides |
| **Origin** | Collapse of chimney material and authigenic mineralization | Slumps | Turbidity currents and plume fall-out |
| **Metal mobilization (except Fe)** | Completed | Ongoing (sulfide leaching) | Ongoing (microbial diagenesis and sulfide oxidation) |
| **Metal preservation** | Fe only | No preservation | Yes, in turbidity layers and by Mn oxide adsorption |
| **Fate** | Source to water column | Sink by mass transport and source by weathering | Sink in the sediments |

**Figure 7.**

at 30 cm depth. At pH < 4.5 the speciation of dissolved inorganic carbon is dominated by its non-dissociated acid form $H_2CO_3$ and consequently alkalinity is zero or negative. Acid attack of sulfide grains is evidenced from pitting and tarnishing of the chalcopyrite crystals in the sulfide sands (Figure 3b). Hence, the increasing concentrations of dissolved $Zn^{2+}$ and $Cu^{2+}$ at depth might be a non-equilibrium process affecting the sulfide minerals. Hence, at the

base of the mounds, the acidic conditions in these distal sediments are likely maintained by the continuous release of acidity from sulfide dissolution within the sediments, leading to the redistribution of some metals. Ingression of oxic seawater, required for the sulfide weathering, might be facilitated by the coarse nature of the sediment (Figure 2).

In the distal channel, the uppermost 60 cm of metalliferous sediments do not show the dissolution of metals into their porewaters, despite having high concentrations of solid phase sulfide. For example, porewater $Co^{2+}$, $Cu^{2+}$, $Mn^{2+}$, and $Zn^{2+}$ concentrations are low despite their high concentrations in the solid phases, especially for $Zn^{2+}$ (e.g., in sphalerite) (38GC in Figure 6c). The absence of these dissolved metals in the porewaters, together with the constant decrease in nitrate with depth, indicates suboxic conditions. Again using TA as indicator of a pH < 4.5 and assuming low organic carbon degradation, these sediments might be less acidic than those at the base of the mounds. In fact, the slight increase in TA could come from the dissolution of carbonates that are present in some of the sediment layers, able to buffer some of the acidity that could be produced during sulfide weathering. Also, the fact that dissolved $Zn^{2+}$ remains low in pore-waters indicates that Zn-containing sulfides are not being oxidized or dissolved in amounts that would lead to a change in pH. This implies that the ingression of oxic seawater into these sediments might be limited, which could be caused by the much finer grained sediment compared to the other environments which have visually coarser sediment textures (Figure 2). In addition, the buried sphalerites may be reworked and protected from further dissolution by an initial oxidative coating (Knight et al., 2017) or they are predominately low-Fe sphalerites, which are more resistant to oxidation (Knight et al., 2017; Weisener et al., 2004). Below a depth of 60 cm, a Mn-rich horizon marks the boundary below which linear increases in concentrations of dissolved $Mn^{2+}$, $Cu^{2+}$, and $Co^{2+}$ with depth in porewaters is indicative of upwards diffusion of these metal ions from deeper horizons (Figure 6c), for example, deeper buried sulfide-rich sands, Mn-oxides, or other sources of metals that can be mobilized. Mn-oxide-rich layers in the sediment suggest the presence of past redox fronts that have stalled before retreating deeper into the sediment column. In summary, in the distal depositional channel, the metal tenor in the sediment is high, deposited through turbidity currents from the nearby hydrothermal mounds before the mound-top material was weathered. Fluids diffusing upwards from a deeper source might have added to the metal tenor. Potentially, the carbonate layers in the sediments can form a pH barrier and might act to preserve the metals and restrict their loss to the water column.

## 6. Conclusions

Our results show how different environments of deposition and processes during and after burial affect the metal content and distribution in TAGHF metalliferous sediments, and how these might be characteristic for near-ridge axis metalliferous sediments in general (Figure 7). These processes are summarized as follows:

1. Weathering: primary hydrothermal sulfides exposed to oxygen-rich seawater will fragment during seafloor weathering and, with increased surface area, the metals are remobilized into porewaters where they are eventually lost to the water column. This extensive weathering of hydrothermal sulfides leads to a depleted metal tenor for the residual sediments found at the mound tops, for example, closest to their origin, resulting in a metal-depleted deposit similar to the gossans described from land.
2. Mass-wasting and turbidity flows: Gravity-driven processes transport some sulfides downslope before they have been weathered, leading to re-distribution and deposition of hydrothermal material away from their sources, for example, in slope sediments and channels. Sediments proximal to their source, such as in the talus and fans at the bases of hydrothermal mounds, are more resistant to alteration and preserve the highest metal concentration in thick beds. This can lead to the retention of thick layers of unsorted sulfides, preserving metals in a higher degree than found elsewhere in the sediments or those more distal to their source. Further away from the source, the rapid burial and the finer-grained nature of the unsorted material reduces the ingress of oxygen-rich seawater and further protects and preserves the original metal tenor of the sediments.

**Figure 7.** Conceptual model and comparative summary for three distinct seafloor environments found at the TAGHF: (a) On top of extinct hydrothermal mounds, the sediment cover is composed of Fe oxyhydroxides originating from prolonged sulfide oxidation, weathering and degradation. Low-temperature fluid flow may be responsible for the formation of Mn-oxide crusts within and on top of the sediments, while seawater infiltration is responsible for acid-induced metal leaching; (b) At the base of extinct hydrothermal mounds, the sediment cover is thin and composed of unsorted Fe-oxyhydroxides mixed with sulfides and secondary weathering minerals (e.g., atacamite and jarosite) provided by collapse or slumps of the hydrothermal mound due to its steep topography. Sulfidic sediments are dominant, metals are mobilized and can be released into the water column (the boundaries between the sediments, silica cap, underlying massive sulfides and the basaltic crust in (a) and (b) are inferred); (c) At further distance, in distal depositional channels, repetitive mass transport and deposition via turbidity events has brought material into depressions where sulfide, oxides and pelagic sediments are accumulated in thin, highly sorted layers. After rapid burial, early diagenesis takes place, oxygen diffuses in the sediments forming an oxic/suboxic boundary where upward diffusing $Mn^{2+}$, $Co^{2+}$, and $Cu^{2+}$ rich porewaters can precipitate solid phases.

3. Diagenetic redistribution: After deposition, the metals in the sediments can be redistributed through diagenetic remobilization, reprecipitating in the sediments or lost to the water column. The degree of diagenesis can depend on the pH, the buffer capacity of carbonate, the reduction of oxygen by organic carbon, and the grain size of the sediment, controlling permeability. Although metals are currently being re-mobilized in porewaters at the TAGHF, high metal contents are retained within thick layers of unsorted sulfides. In addition, upward advection of metal-enriched low-temperature hydrothermal fluids or diffusion of metal-enriched fluids from deeper layers could lead to additional accumulation of metals at redox boundaries after the high-temperature activity has ceased.
4. Plume fallout: Close to inactive hydrothermal mounds, the plume fallout signal might be concealed due to high metal contents and rapid deposition of mound-top material with the remobilization of metals in the sediments. This can yield false results in terms of identifying potential hydrothermal events.

In conclusion, although physical transport and deposition is one of the main drivers for solid phase metal concentrations in hydrothermal sediments, diagenetic processes and fluids from different sources can overprint the inherited metal tenor. These processes may be important when sediments are used as vectors to hydrothermal deposits, since the highest metal content in sediments is not necessarily found primarily in closest proximity to the deposit source. Similarly, not only metal content and concentrations of sediments should be used for provenance discrimination, but grain size, sediment texture and even seafloor morphology (e.g., sediment ponds) should also be considered. Our findings might particularly be interesting for studies that use near-vent sediments to reconstruct the history of the hydrothermal activity (e.g., Li et al., 2023; Lund et al., 2016; Middleton et al., 2016; Qiu et al., 2021). These studies are based on the premise that metal-enriched layers (especially Mn and Fe) within the sediment column are the result of fall-out from hydrothermal plumes and hence their presence in the stratigraphic record indicates periods of hydrothermal activity. To obtain a reliable record from metalliferous layers requires identifying the difference between primary plume fall-out, reworking by mass-wasting and transport, and redox-driven precipitation following dissolution and remobilization from underlying metalliferous sediments. We recommend that these processes and their implications for the provenance of the metalliferous layers should be taken into account before a reliable age model of hydrothermal activity can be constructed. While areas where sediments have clearly been transported (e.g., at the base of the mounds), and proximal where the likelihood of mobilizing metals from underlying metalliferous sediments is high (e.g., on the tops of hydrothermal mounds), might be less suitable for geochronological reconstruction of hydrothermal activity, the most promising locations are more likely to be in small topographic lows or highs on the seafloor, far from any hydrothermal edifice, were plume fall-out and mass-wasting transport can easily be distinguished.

## Data Availability Statement

All presented results are available in the Pangaea data base (Dutrieux, 2020, https://doi.pangaea.de/10.1594/PANGAEA.922078). In addition, Co, Cu, and Zn content of sulfides previously collected from TAG nearby sulfides mounds are presented in Table S1 of Supporting Information S1.

**Acknowledgments**
The authors acknowledge support from the European Union FP7 Grant 604500 "Blue Mining." The authors would also like to gratefully acknowledge the JC138 shipboard party, the HyBIS and the BGS RD2 rock drill technical support team for their assistance during the expedition. The authors acknowledge Geomar Abyss AUV team, Sven Petersen, and Sebastian Graber for providing ship-based bathymetric data of cruise M127. We also thank Matt Cooper, Kate Peel, and Richard Pearce for their help with geochemical analyses, Pierre Josso for helpful discussions and the reviewers for their constructive support. The British Ocean Sediment Core Research Facility (BOSCORF) is thanked for using their facilities. FB, SM, and JM would like to acknowledge the financial support of FCT through project UIDB/50019/2020—IDL. This work was supported by a PhD studentship to AMD from the Graduate School of the National Oceanography Centre Southampton.

## References

Barriga, F. J. A. S., & Carvalho, D. (1983). Carboniferous volcanogenic sulphide mineralizations in South Portugal (Iberian Pyrite Belt). *Carboniferous of Portugal* (pp. 99–113).

Barton, P. B., & Bethke, P. M. (1987). Chalcopyrite disease in sphalerite; pathology and epidemiology. *American Mineralogist*, *72*, 451–467.

Bertram, C., Krätschell, A., O'Brien, K., Brückmann, W., Proelss, A., & Rehdanz, K. (2011). Metalliferous sediments in the Atlantis II Deep—Assessing the geological and economic resource potential and legal constraints. *Resources Policy*, *36*(4), 315–329. https://doi.org/10.1016/j.resourpol.2011.09.001

Bortnikov, N. S., Genkin, A. D., Dobrovol'skaya, M. G., Muravitskaya, G. N., & Filimonova, A. A. (1991). The nature of chalcopyrite inclusions in sphalerite: Exsolution, coprecipitation, or "disease''? *Economic Geology*, *86*(5), 1070–1082. https://doi.org/10.2113/gsecongeo.86.5.1070

Bouma, A. (1962). *Sedimentology of some flysch deposits: A graphic approach to facies interpretation* (p. 168). Elsevier.

Cline, J. D. (1969). Spectrophotometric determination of hydrogen sulfide in natural waters. *Limnology and Oceanography*, *14*(3), 454–458. https://doi.org/10.4319/lo.1969.14.3.0454

Croudace, I. W., Rindby, A., & Rothwell, R. G. (2006). ITRAX: Description and evaluation of a new multi-function X-ray core scanner. *Geological Society, London, Special Publications*, *267*(1), 51–63. https://doi.org/10.1144/gsl.sp.2006.267.01.04

de Martin, B. J., Sohn, R. A., Canales, J. P., & Humphris, S. E. (2007). Kinematics and geometry of active detachment faulting beneath the Trans-Atlantic Geotraverse (TAG) hydrothermal field on the Mid-Atlantic Ridge. *Geology*, *35*(8), 711–714. https://doi.org/10.1130/g23718a.1

Dilek, Y., Moores, E. M., Elthon, D., & Nicolas, A. (Eds.). (2000). *Ophiolites and oceanic crust: New insights from field studies and the ocean drilling program* (Vol. 349, pp. 213–235). Geological Society of America.

Douville, E., Bienvenu, P., Charlou, J.-L., Donval, J.-P., Fouquet, Y., Appriou, P., & Gamo, T. (1999). Yttrium and rare earth elements in fluids from various deep-sea hydrothermal systems. *Geochimica et Cosmochimica Acta*, *63*(5), 627–643. https://doi.org/10.1016/s0016-7037(99)00024-1

Dutrieux, A. M. (2020). Diverse analytical data (i.e. Geochemistry and mineralogy) on metalliferous sediments and pore waters in hydrothermal sediments at the TAG Hydrothermal Field from sediment cores of James Cook cruise JC138 [Dataset]. PANGAEA. https://doi.org/10.1594/PANGAEA.922078

Elderfield, H. (1988). The oceanic chemistry of the rare-earth elements. *Philosophical Transactions of the Royal Society of London - Series A: Mathematical and Physical Sciences*, *325*, 105–126.

Evensen, N. M., Hamilton, P. J., & O'Nions, R. K. (1978). Rare-earth abundances in chondritic meteorites. *Geochimica et Cosmochimica Acta*, *42*(8), 1199–1212. https://doi.org/10.1016/0016-7037(78)90114-x

German, C. R., Higgs, N. C., Thomson, J., Mills, R. A., Elderfield, H., Blusztajn, J., et al. (1993). A geochemical study of metalliferous sediment from the TAG Hydrothermal Mound, 26°08′N, Mid-Atlantic Ridge. *Journal of Geophysical Research*, *98*(B6), 9683. https://doi.org/10.1029/92jb01705

German, C. R., Klinkhammer, G. P., Edmond, J. M., Mura, A., & Elderfield, H. (1990). Hydrothermal scavenging of rare-earth elements in the ocean. *Nature*, *345*(6275), 516–518. https://doi.org/10.1038/345516a0

Glynn, S., Mills, R. A., Palmer, M. R., Pancost, R. D., Severmann, S., & Boyce, A. (2006). The role of prokaryotes in supergene alteration of submarine hydrothermal sulfides. *Earth and Planetary Science Letters*, *244*(1–2), 170–185. https://doi.org/10.1016/j.epsl.2006.01.065

Goulding, H. C., Mills, R. A., & Nesbitt, R. W. (1998). Precipitation of hydrothermal sediments on the active TAG Mound; implications for ochre formation. In R. A. Mills & K. Harrison (Eds.), *Modern ocean floor processes and the geological record* (pp. 201–216). Geological Society of London.

Grasshoff, K., Ehrhardt, M., & Kremling, K. (1983). In K. Grasshoff, M. Ehrhardt, & K. Kremling (Eds.), *Methods of seawater analysis*. Verlag Chemic GmbH.

Griffith, E. M., & Paytan, A. (2012). Barite in the ocean - Occurrence, geochemistry and palaeoceanographic applications. *Sedimentology*, *59*(6), 1817–1835. https://doi.org/10.1111/j.1365-3091.2012.01327.x

Gurvich, E. G. (2006). *Metalliferous sediments of the world ocean: Fundamental theory of deep-sea hydrothermal sedimentation*. Springer-Verlag Berlin Heidelberg.

Hannington, M. D., Galley, A. G., Herzig, P. M., & Petersen, S. (1998). Comparison of the TAG mound and stockwork complex with Cyprus-type massive sulphide deposits. *Proceedings of the Ocean Drilling Program - Scientific Results*, *158*, 389–415.

Hannington, M. D., Jamieson, J. W., Monecke, T., Petersen, S., & Beaulieu, S. E. (2011). The abundance of seafloor massive sulfide deposits. *Geology*, *39*(12), 1155–1158. https://doi.org/10.1130/g32468.1

Hannington, M. D., Petersen, S., Herzig, P. M., & Jonasson, I. (2004). A global database of seafloor hydrothermal systems, including a digital database of geochemical analyses of seafloor polymetallic sulfides: Geological Survey of Canada, Open File 4598, 1 CD-ROM. Retrieved from http://oceanrep.geomar.de/33243/1/Hannington.pdf

Hansell, D. A., & Follows, M. J. (2008). Nitrogen in the Atlantic Ocean. *Nitrogen in the marine environment* (pp. 597–630).

Hein, J. R., Clague, D. A., Koski, R. A., Embley, R. W., & Dunham, R. E. (2008). Metalliferous sediment and a silica-hematite deposit within the Blanco Fracture Zone, northeast Pacific. *Marine Georesources & Geotechnology*, *26*(4), 317–339. https://doi.org/10.1080/10641190802430986

Humphris, S. E., & Tivey, M. K. (2000). *A synthesis of geological and geochemical investigations of the TAG hydrothermal field: Insights into fluid-flow and mixing processes in a hydrothermal system* (pp. 213–236). Special Papers-Geological Society of America.

Josso, P., Pelleter, E., Pourret, O., Fouquet, Y., Etoubleau, J., Cheron, S., & Bollinger, C. (2017). A new discrimination scheme for oceanic ferromanganese deposits using high field strength and rare earth elements. *Ore Geology Reviews*, *87*, 3–15. https://doi.org/10.1016/j.oregeorev.2016.09.003

Klinkhammer, G. P., Elderfield, H., Edmond, J. M., & Mitra, A. (1994). Geochemical implications of rare earth elements patterns in hydrothermal fluids from mid-ocean ridges. *Geochimica et Cosmochimica Acta*, *58*(23), 5105–5113. https://doi.org/10.1016/0016-7037(94)90297-6

Knight, R. D., Roberts, S., & Cooper, M. J. (2017). Investigating monomineralic and polymineralic reactions during the oxidation of sulphide minerals in seawater: Implications for mining seafloor massive sulphide deposits. *Applied Geochemistry*, *90*, 63–74. https://doi.org/10.1016/j.apgeochem.2017.12.027

Krasnov, S. G., Cherkashov, G. A., Stepanova, T. V., Batuyev, B. N., Krotov, a. G., Malin, B. V., et al. (1995). Detailed geological studies of hydrothermal fields in the North Atlantic. *Geological Society, London, Special Publications*, *87*(1), 43–64. https://doi.org/10.1144/gsl.sp.1995.087.01.05

Li, M., Han, X., Qiu, Z., Fan, W., Wang, Y., Li, H., et al. (2023). Sea-level fall driving enhanced hydrothermal and tectonic activities: Evidence from a sediment core near the tectonic-controlled Tianxiu Vent Field, Carlsberg Ridge. *Geophysical Research Letters*, *50*(7), e2022GL101599. https://doi.org/10.1029/2022gl101599

Liao, S., Tao, C., Li, H., Zhang, G., Liang, J., Yang, W., & Wang, Y. (2018). Surface sediment geochemistry and hydrothermal activity indicators in the Dragon Horn area on the Southwest Indian Ridge. *Marine Geology*, *398*, 22–34. https://doi.org/10.1016/j.margeo.2017.12.005

Lichtschlag, A., James, R. H., Stahl, H., & Connelly, D. P. (2015). Effect of a controlled sub-seabed release of $CO_2$ on the biogeochemistry of shallow marine sediments, their pore waters, and the overlying water column. *International Journal of Greenhouse Gas Control*, *38*, 80–92. https://doi.org/10.1016/j.ijggc.2014.10.008

Lund, D. C., Asimow, P. D., Farley, K. A., Rooney, T. O., Seeley, E., Jackson, E. W., & Durham, Z. M. (2016). Enhanced East Pacific Rise hydrothermal activity during the last two glacial terminations. *Science*, *351*(6272), 478–482. https://doi.org/10.1126/science.aad4296

Metz, S., Trefry, J. H., & Nelsen, T. A. (1988). History and geochemistry of a metalliferous sediment core from the Mid-Atlantic Ridge at 26°N. *Geochimica et Cosmochimica Acta*, *52*(10), 2369–2378. https://doi.org/10.1016/0016-7037(88)90294-3

Middleton, J., Langmuir, C. H., Mukhopadhyay, S., McManus, J. F., & Mitrovica, J. X. (2016). Hydrothermal iron flux variability following rapid sea level changes. *Geophysical Research Letters*, *43*(8), 3848–3856. https://doi.org/10.1002/2016gl068408

Milinovic, J., Dias, Á. A., Janeiro, A. I., Pereira, M. F., Martins, S., Petersen, S., & Barriga, F. J. A. S. (2020). XRD identification of ore minerals during cruises: Refinement of extraction procedure with sodium acetate buffer. *Minerals*, *10*(2), 160. https://doi.org/10.3390/min10020160

Mills, R. A., Clayton, T., & Alt, J. C. (1996). Low-temperature fluid flow through sulfidic sediments from TAG: Modification of fluid chemistry and alteration of mineral deposits. *Geophysical Research Letters*, *23*, 3495–3498. https://doi.org/10.1029/96gl02885

Mills, R. A., & Elderfield, H. (1995). Rare earth element geochemistry of hydrothermal deposits from the active TAG Mound, 26°N Mid-Atlantic Ridge. *Geochimica et Cosmochimica Acta*, *59*(17), 3511–3524. https://doi.org/10.1016/0016-7037(95)00224-n

Mills, R. A., Elderfield, H., & Thomson, J. (1993). A dual origin for the hydrothermal component in a metalliferous sediment core from the Mid-Atlantic Ridge. *Journal of Geophysical Research*, *98*(B6), 9671–9681. https://doi.org/10.1029/92jb01414

Mitra, A., Elderfield, H., & Greaves, M. J. (1994). Rare earth elements in submarine hydrothermal fluids and plumes from the Mid-Atlantic Ridge. *Marine Chemistry*, *46*(3), 217–235. https://doi.org/10.1016/0304-4203(94)90079-5

Müller, M., Handley, K. M., Lloyd, J., Pancost, R. D., & Mills, R. A. (2010). Biogeochemical controls on microbial diversity in seafloor sulphidic sediments. *Geobiology*, *8*(4), 309–326. https://doi.org/10.1111/j.1472-4669.2010.00242.x

Murton, B. J., Lehrmann, B., Dutrieux, A. M., Martins, S., Gil de la Iglesia, A., Stobbs, I. J., et al. (2019). Geological fate of seafloor massive sulphides at the TAG hydrothermal field (Mid-Atlantic Ridge). *Ore Geology Reviews*, *107*, 903–925. https://doi.org/10.1016/j.oregeorev.2019.03.005

Petersen, S. (2000). *The geochemical and mineralogical evolution of the TAG Hydrothermal Field, Mid-Atlantic Ridge, 26°N*. Technische Universität Bergakademie Freiberg.

Petersen, S. (2019). Bathymetric data products from AUV dives during METEOR cruise M127 (TAG Hydrothermal Field, Atlantic) [Dataset]. PANGAEA. https://doi.org/10.1594/PANGAEA.899415

Petersen, S., & Scientific Party, S. (2016). RV METEOR Fahrtbericht/Cruise Report M127 - Extended Version: Metal fluxes and resource potential at the slow-spreading TAG Mid-ocean ridge segment (26°N, MAR) – Blue Mining@Sea (pp. 1–59).

Qiu, Z., Han, X., Li, M., Wang, Y., Cheng, X., Fan, W., et al. (2021). The temporal variability of hydrothermal activity of Wocan hydrothermal field, Carlsberg Ridge, northwest Indian Ocean. *Ore Geology Reviews*, *132*, 103999. https://doi.org/10.1016/j.oregeorev.2021.103999

Rona, P. A., Bogdanov, Y. A., Gurvich, E. G., Rimski-Korsakov, N. A., Sagalevitch, A. M., Hannington, M. D., & Thompson, G. (1993). Relict hydrothermal zones in the TAG Hydrothermal Field, Mid-Atlantic Ridge 26°N, 45°W. *Journal of Geophysical Research*, *98*(B6), 9715–9730. https://doi.org/10.1029/93jb00552

Rona, P. A., Hannington, M. D., Raman, C. V., Thompson, G., Tivey, M. K., Humphris, S. E., et al. (1993). Active and relict sea-floor hydrothermal mineralization at the TAG hydrothermal field, Mid-Atlantic Ridge. *Economic Geology*, *88*(8), 1989–2017. https://doi.org/10.2113/gsecongeo.88.8.1989

Scott, M. R., Scott, R. B., Morse, J. W., Betzer, P. R., Butler, L. W., & Rona, P. A. (1978). Metal-enriched sediments from the TAG Hydrothermal Field. *Nature*, *276*(5690), 811–813. https://doi.org/10.1038/276811a0

Scott, R. B., Rona, P. A., McGregor, B. A., & Scott, M. R. (1974). The TAG hydrothermal field. *Nature*, *248*(5473), 81–82. https://doi.org/10.1038/251301a0

Seeberg-Elverfeldt, J., Schluter, M., Feseker, T., & Kolling, M. (2005). Rhizon sampling of porewaters near the sediment-water interface of aquatic systems. *Limnol. Oceanogr.*, *3*(8), 361–371. https://doi.org/10.4319/lom.2005.3.361

Severmann, S., Mills, R. A., Palmer, M. R., Telling, J. P., Cragg, B. A., & John Parkes, R. (2006). The role of prokaryotes in subsurface weathering of hydrothermal sediments: A combined geochemical and microbiological investigation. *Geochimica et Cosmochimica Acta*, *70*(7), 1677–1694. https://doi.org/10.1016/j.gca.2005.12.008

Shanmugam, G. (2018). Slides, slumps, debris flows, turbidity currents, hyperpycnal flows, and bottom currents. In *Reference module in Earth systems and environmental sciences*. Elsevier.

Shearme, S., Cronan, D. S., & Rona, P. A. (1983). Geochemistry of sediments from the TAG Hydrothermal Field, M.A.R. at latitude 26°N. *Marine Geology*, *51*(3–4), 269–291. https://doi.org/10.1016/0025-3227(83)90108-1

Thompson, G., Mottl, M. J., & Rona, P. A. (1985). Morphology, mineralogy and chemistry of hydrothermal deposits from the TAG area, 2°N, Mid-Atlantic Ridge. *Chemical Geology*, *49*(1–3), 243–257. https://doi.org/10.1016/0009-2541(85)90159-7

Webber, A. P., Roberts, S., Murton, B. J., & Hodgkinson, M. R. S. (2015). Geology, sulfide geochemistry and supercritical venting at the Beebe Hydrothermal Vent Field, Cayman Trough. *Geochemistry, Geophysics, Geosystems*, *16*(8), 2661–2678. https://doi.org/10.1002/2015gc005879

Weisener, C. G., Smart, R. S. C., & Gerson, A. R. (2004). A comparison of the kinetics and mechanism of acid leaching of sphalerite containing low and high concentrations of iron. *International Journal of Mineral Processing*, *74*(1–4), 239–249. https://doi.org/10.1016/j.minpro.2003.12.001

White, S. N., Humphris, S. E., & Kleinrock, M. C. (1998). New observations on the distribution of past and present hydrothermal activity in the TAG area of the Mid-Atlantic Ridge (26°08′N). *Marine Geophysical Researches*, *20*(1), 41–56. https://doi.org/10.1023/a:1004376229719